IOP Publishing Phys. Med. Biol. 64 (2019) 074001 (11pp) https://doi.org/10.1088/1361-6560/ab0fc9

Physics in Medicine & Biology

IPEM Institute of Physics and Engineering in Medicine

PAPER

Discriminating nanoparticle core size using multi-contrast MPI

Carolyn Shasha[1,5], Eric Teeman[2], Kannan M Krishnan[1,2], Patryk Szwargulski[3,4], Tobias Knopp[3,4] and Martin Möddel[3,4]

[1] Department of Physics, University of Washington, Seattle, Washington, United States of America
[2] Department of Materials Sciences & Engineering, University of Washington, Seattle, Washington, United States of America
[3] Section for Biomedical Imaging, University Medical Center Hamburg-Eppendorf, Hamburg, Germany
[4] Institute for Biomedical Imaging, Hamburg University of Technology, Hamburg, Germany
[5] Author to whom any correspondence should be addressed.

E-mail: cshasha@uw.edu

RECEIVED
27 December 2018

REVISED
4 March 2019

ACCEPTED FOR PUBLICATION
14 March 2019

PUBLISHED
29 March 2019

Keywords: magnetic particle imaging, multi-contrast magnetic particle imaging, functional imaging, magnetic nanoparticles, magnetic particle spectroscopy

Abstract

Magnetic particle imaging (MPI) is an imaging modality that detects the response of a distribution of magnetic nanoparticle tracers to alternating magnetic fields. There has recently been exploration into multi-contrast MPI, in which the signal from different tracer materials or environments is separately reconstructed, resulting in multi-channel images that could enable temperature or viscosity quantification. In this work, we apply a multi-contrast reconstruction technique to discriminate between nanoparticle tracers of different core sizes. Three nanoparticle types with core diameters of 21.9 nm, 25.3 nm and 27.7 nm were each imaged at 21 different locations within the scanner field of view. Multi-channel images were reconstructed for each sample and location, with each channel corresponding to one of the three core sizes. For each image, signal weight vectors were calculated, which were then used to classify each image by core size. With a block averaging length of 10 000, the median signal-to-noise ratio was 40 or higher for all three sample types, and a correct prediction rate of 96.7% was achieved, indicating that core size can effectively be predicted using signal weight vector classification with close to 100% accuracy while retaining high MPI image quality. The discrimination of the core size was reliable even when multiple samples of different core sizes were placed in the measuring field.

1. Introduction

Magnetic particle imaging (MPI) is an emerging tomographic medical imaging platform which employs static and dynamic magnetic fields. In MPI, the excitation response of magnetic nanoparticles (MNPs) is recorded, allowing for spatial encoding of MNP distribution using gradient fields (Gleich and Weizenecker 2005, Weizenecker *et al* 2009, Krishnan 2010). In principle, magnetic nanoparticle tracers in aqueous solution would be administered intravenously and allowed to circulate throughout the body, enabling high-resolution cardiovascular imaging with high sensitivity. Recently, there has been exploration into the possibility of multi-contrast (also referred to as 'multi-color' or 'colored') MPI, in which the signal from different tracers or tracer environments is separated (Rahmer *et al* 2015). In standard frequency-space MPI, the image is reconstructed from the induced voltage signal using a single system function, which is the kernel to the integral imaging equation (Rahmer *et al* 2009). With multi-contrast MPI, multiple system functions are used for image reconstruction, resulting in multi-channel images. A detailed theoretical description of multi-contrast frequency-space MPI can be found in Möddel *et al* (2018).

Tracer properties and properties of the local particle environment that influence the tracer relaxation behavior include temperature, viscosity, mobility state, material, and core/hydrodynamic size. Several of these have recently been investigated using magnetic particle spectroscopy (MPS) and 1D and 2D MPI (Rauwerdink and Weaver 2009, 2010, Rauwerdink *et al* 2010, Wawrzik *et al* 2013, Hensley *et al* 2015, Rahmer *et al* 2015, Utkur *et al* 2017), most notably quantitative viscosity imaging in Möddel *et al* (2018), qualitative temperature mapping in Stehning *et al* (2016) and quantitative temperature mapping in Zhong *et al* (2018) and Wells *et al* (2018). In this

work, we investigate the potential for multi-contrast MPI using MNP core size differentiation. Past demonstrations of multi-contrast MPI based on tracer, rather than environment, discrimination involved nanoparticle tracers that did not display optimized MPI performance, primarily due to high polydispersity and non-optimal sizes. With highly tailored single-core MNPs specifically designed for optimal MPI performance, as defined by image resolution and signal intensity, MNP cores of different sizes could be separately functionalized for specific purposes, e.g. long-term circulation (Khandhar *et al* 2017), cancer targeting (Arami *et al* 2017), or coating of devices for cardiovascular interventions (Panagiotopoulos *et al* 2015, Salamon *et al* 2016), allowing for reconstruction of high resolution images with high sensitivity on each channel. While the focus of this work is MPI, it should be mentioned that multicolor image reconstruction has been studied for other nanoparticle-based imaging methods as well. For example, fluorescence-based multicolor bioimaging using biosynthesized zinc nanoparticles was shown in Kang *et al* (2017), and multicolor imaging using magnetorelaxometry with 200 nm–500 nm nanoparticles was demonstrated in Coene *et al* (2017).

Due to its biocompatibility, iron oxide is the typical material used for MNP tracers, particularly the magnetite phase, which has the highest saturation magnetization (446 kA m^{-1}). The optimal size range for MPI performance of phase-pure magnetite tracers has been experimentally determined to be 23 nm–28 nm in core diameter (Ferguson *et al* 2013, 2015). Below diameters of about 23 nm, particles require a higher applied field strength to saturate, resulting in lower recorded signal. Above approximately 28 nm, the phase lag between the drive-field and particle response becomes large and the particle magnetization can no longer follow the field, resulting in decreased image resolution. Due to this size restriction, a size-based differentiation approach requires highly monodisperse particles with carefully controlled size, as well as a highly sensitive signal separation technique.

For particles in this size range (23 nm–28 nm core diameter) under an applied AC field, a combination of Néel relaxation (flipping of the magnetic moment within the particle) and Brownian relaxation (rotation of the entire particle to align with the field) may occur, depending on the particle hydrodynamic size (Deissler *et al* 2014, Shah *et al* 2015). In this work, we adapt the experimental part of Möddel *et al* (2018) to demonstrate particle size discrimination and combine it with sample localization in 2D MPI using highly monodisperse optimized MNPs.

2. Experimental setup

At the core of our discrimination experiment we have three particle types with different core sizes. In the following we provide a detailed description of the particle synthesis and outline the magnetic particle spectroscopy and imaging experiments.

2.1. Particle synthesis

Magnetite nanoparticles were synthesized according to a thermal decomposition process using an iron oleate precursor, as described in detail in Kemp *et al* (2016). The iron oleate was produced by dissolving a solution of iron (III) chloride and sodium oleate in hexanes, ethanol, and deionized water and heated under argon for four hours at reflux. The resultant product was extracted in a separating funnel and the aqueous layer was removed. The organic layer was washed with deionized water and dried with sodium sulfate. The remaining solvent was removed by rotary evaporation. The iron oleate was dissolved in 1-octadecene and oleic acid and heated under argon to 324 °C until nucleation. The temperature was then lowered to 318 °C and mixture exposed to a 1% oxygen/99% argon atmosphere until particles had grown to desired size.

Three particle types, S, M, and L, were fabricated, with core diameters of 21.9 nm, 25.3 nm and 27.7 nm and respective distribution parameters of 0.04, 0.08 and 0.07. Particle diameters were assumed to follow a log-normal distribution. Size, size distribution, and crystallographic phase were determined with transmission electron microscopy (TEM), by preparing samples on 200-mesh carbon coated copper grids from a 1 mg ml^{-1} nanoparticle solution in chloroform. Particle sizes and distributions were determined from TEM images using ImageJ open source software.

The nanoparticle cores were made dispersible in aqueous medium by coating with an amphiphilic co-polymer comprised of polyethylene glycol and poly(maleic anhydride- *alt*-1-octadecene). Hydrodynamic sizes of dispersions in deionized water were determined by dynamic light scattering (DLS) resulting in sizes of 94.3 nm, 77.1 nm and 95.9 nm, with respective distribution parameters of 0.13, 0.18 and 0.15. Particles were then normalized to a concentration of 0.9_{gFe} l^{-1}, confirmed by inductively coupled plasma—optical emission spectrometry (ICP-OES).

2.2. Magnetic particle spectroscopy

MPS measurements were taken using a custom-built spectrometer (Ferguson *et al* 2012) with a drive frequency of 26 kHz and a drive-field amplitude of 20 mT μ_0^{-1}, where μ_0 is the vacuum permeability. The tracer magnetization response, dm/dt, is recorded as the induced voltage in the receive coil caused by a sinusoidal excitation field H. The receive circuit has an upper frequency of 1.04 MHz, allowing detection of up to 40 harmonics after Fourier

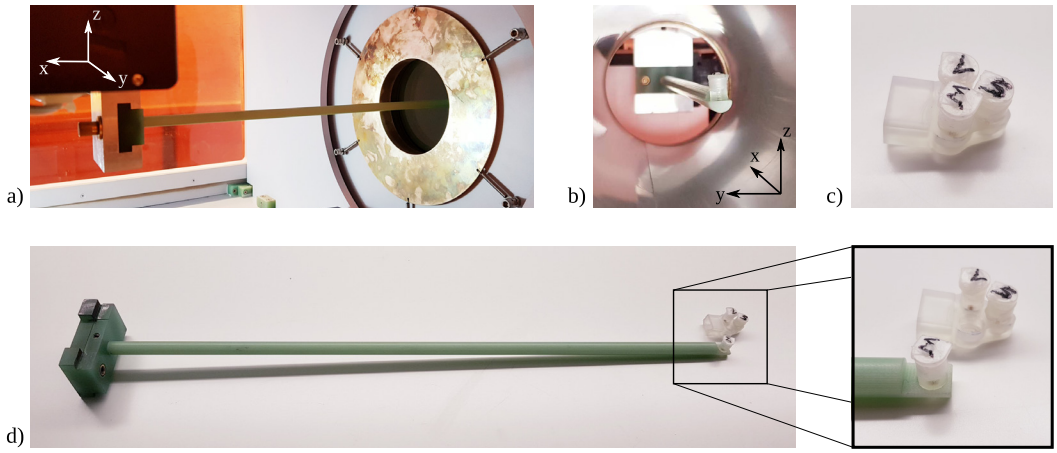

Figure 1. In (a) and (b) the three axis robot and the rod used to move the sample within the scanner bore are shown in back and front view, respectively. (c) shows the sample holder used for the multi-sample experiments with all three samples mounted on the holder. Each sample as well as the sample holder can be mounted on the rod for a precise positioning within the scanner bore (d).

transform. Measurements of 150 μl aqueous solutions of particle types, S, M, and L were performed in triplicate, and were then averaged.

2.3. Magnetic particle imaging

Multi-contrast MPI is performed using a preclinical MPI scanner (Philips preclinical MPI package with a Bruker preclinical MPI system) (Bruker Biospin MRI GmbH Ettlingen, Germany 2015). All samples are moved within the scanner using a three axis robot (isel automation GmbH) positioned in the back of the scanner shown in figure 1(a). The view into the scanner bore with a mounted sample on the robot rod is shown in figure 1(b). For imaging, a 2D FoV of 20 mm $\times$ 20 mm in the xy-plane is used, which lies horizontally within the scanner gantry. Particle excitation is done using drive-fields with frequencies of 2.5/102 MHz and 2.5/96 MHz and amplitudes of 12 mT μ_0^{-1} in the x- and y-direction. With these parameters, a single scan of the 2D FoV takes 652.8 μs. Spatial encoding uses a gradient field of 1.2 $\mu_0^{-1}\,\mathrm{m}^{-1}$, 1.2 $\mu_0^{-1}\,\mathrm{m}^{-1}$ and 2.4$\mu_0^{-1}\,\mathrm{m}^{-1}$ in the x-, y-, and z-direction. During excitation, the particles' magnetization signal is recorded by three orthogonal pick up coils aligned along the x-, y- and z-direction. The three signals are filtered and digitized with a bandwidth of 1.25 MHz. The final measurement vector contains the Fourier transformed time signals from each location.

A cuboid-shaped 1 mm $\times$ 1 mm $\times$ 2 mm sample was prepared from each of the particle solutions. These samples are labeled S, M, and L corresponding to the particle sample they contain. In total three system matrix, three regular MPI measurements with a single sample, and four regular MPI measurements with multiple samples in the FoV were performed.

The three system matrix measurements were performed on a 24 mm $\times$ 24 mm field of view with a voxel size of 1 mm $\times$ 1 mm by averaging 10 000 measurements at each grid position for each sample. The data from each measurement was processed into a system matrix. Henceforth, we refer to the system matrices to as $\mathbf{S}_\mathrm{S}$, $\mathbf{S}_\mathrm{M}$, and $\mathbf{S}_\mathrm{L}$ corresponding to the samples S, M, and L respectively. In a series of three independent experiments each sample was attached to the arm of a three axis robot and moved to the center position of the scanner and 20 additional uniform random positions within the FoV. At each position 10 000 measurements were taken. The random positions were the same for each of the three experiments and are listed in table 1 and shown in figure 2.

In the final experiment different combinations of all three samples were scanned simultaneously. To this end, a sample holder containing the samples was mounted to the robot and moved to the center of the FoV. The arrangement is shown in figures 1(c) and (d). In four independent scans first all three samples and afterwards all three combinations of two samples were measured. Each measurement contains 10 000 frames.

3. Multi-contrast MPI core size discrimination

The particles' core sizes within a sample are discriminated in a three-step procedure. These steps are adapted from our earlier work on viscosity quantification (Möddel *et al* 2018). The first step, multi-channel image reconstruction, is modified only slightly and will be briefly summarized in the following subsection. Second and third, image processing and core size discrimination are outlined thereafter in a separate subsection. Additionally, we estimate image SNR and sample size as described in the last subsection.

Table 1. A table with all sample positions.

Position	0	1	2	3	4	5	6	7	8	9	10
x (mm)	0.00	−3.87	−5.54	0.84	3.03	7.32	8.34	0.71	−6.33	1.58	2.45
y (mm)	0.00	−8.32	−3.12	−5.46	1.19	8.68	−7.49	−3.37	0.93	−7.35	−2.62

Position	11	12	13	14	15	16	17	18	19	20
x (mm)	−7.23	5.57	−1.54	7.65	2.95	−1.03	5.15	−3.16	−8.21	2.62
y (mm)	1.58	−0.05	−3.78	7.6	3.93	4.36	3.31	0.2	7.47	6.31

3.1. Multi-channel image reconstruction

Prior to reconstruction, measurements and system matrices are frequency filtered, i.e. only frequencies above 80 kHz and with a signal to noise ratio above 3.5 are used for reconstruction. To analyze the influence of noise on the size discrimination the measurements obtained at each position were block averaged with a block length M_{avg} of 10 000, 1000 and 100 yielding 1, 10 and 100 final multi-channel images per sample and position.

Using the system matrices $\mathbf{S}_{\text{S}}$, $\mathbf{S}_{\text{M}}$, and $\mathbf{S}_{\text{L}}$ a multi-channel image reconstruction was performed by solving the Tikhonov regularized optimization problem

$$\mathbf{c}_{\text{S}}, \mathbf{c}_{\text{M}}, \mathbf{c}_{\text{L}} = \underset{\tilde{\mathbf{c}}_{\text{S}}, \tilde{\mathbf{c}}_{\text{M}}, \tilde{\mathbf{c}}_{\text{L}} \in \mathbb{R}_{+}^{N}}{\operatorname{argmin}} \left\| \begin{pmatrix} \mathbf{S}_{\text{S}} & \mathbf{S}_{\text{M}} & \mathbf{S}_{\text{L}} \end{pmatrix} \begin{pmatrix} \tilde{\mathbf{c}}_{\text{S}} \\ \tilde{\mathbf{c}}_{\text{M}} \\ \tilde{\mathbf{c}}_{\text{L}} \end{pmatrix} - \hat{\mathbf{u}} \right\|_2^2 + \tilde{\lambda} \left\| \begin{pmatrix} \tilde{\mathbf{c}}_{\text{S}} \\ \tilde{\mathbf{c}}_{\text{M}} \\ \tilde{\mathbf{c}}_{\text{L}} \end{pmatrix} \right\|_2^2 \tag{1}$$

for each measurement vector $\hat{\mathbf{u}}$ (Rahmer *et al* 2015). Here, $N = 24 \times 24$ is the total number of voxels within each channel and $\tilde{\lambda}$ is the Tikhonov regularization parameter. The latter is usually not directly reported, but $\tilde{\lambda} = \lambda N / \| \begin{pmatrix} \mathbf{S}_{\text{S}} & \mathbf{S}_{\text{M}} & \mathbf{S}_{\text{L}} \end{pmatrix} \|_F$, where $\| \cdot \|_F$ denotes the Frobenius-norm. The channels $\mathbf{c}_{\text{S}}$, $\mathbf{c}_{\text{M}}$, and $\mathbf{c}_{\text{L}}$ are obtained by iteratively solving equation (1) using 10 000 iterations of the Kaczmarz solver. The regularization parameter λ for the single sample measurements was chosen to be 0.01, 0.05 and 0.1 for M_{avg} of 10 000, 1000 and 100, respectively. In case of the multi-sample measurements the averaging was set to $M_{\text{avg}} = 10\,000$ and the regularization parameter λ was set to 10^{-4}.

3.2. Core size discrimination

As shown in figure 3 each reconstructed image contains the channels $\mathbf{c}_{\text{S}}$, $\mathbf{c}_{\text{M}}$ and $\mathbf{c}_{\text{L}}$. The signal generated by the samples within the different channels is collected by summation over a circular region of interest (ROI) for each channel individually, shown in figure 4. The ROI is centered at the corresponding sample position and has a radius of 4 voxels clipped against the edges of the reconstructed images. The resulting summation yields a weights vector $w = (\sigma_{\text{S}}, \sigma_{\text{M}}, \sigma_{\text{L}}) \in \mathbb{R}_{+}^{3}$ containing the summed signal for the channels $\mathbf{c}_{\text{S}}$, $\mathbf{c}_{\text{M}}$, and $\mathbf{c}_{\text{L}}$, respectively.

Reconstruction parameters are different for each block averaging length. Therefore, we split our data with respect to the block averaging length into three independent sets. Note that the core size discrimination algorithm described here will be applied to each set individually. Weight vectors $w_{s,p,i}$ are calculated for all samples $s \in \{\text{S}, \text{M}, \text{L}\}$, positions $p \in \{0, 1, \ldots, 20\}$ and each image i. Taking the weight vectors $w_{s,p,i}$ as observations, the task of core size discrimination can be formulated as a classification problem, where we have to identify a suitable core size label, i.e. S, M, or L, for each observation. Here, we use the nearest centroid classification algorithm for this task. This algorithm is split into two parts: a learning phase and a classification phase. In the learning phase we use the weight vectors $w_{s,p=0,i}$ and class labels s as training data to calculate the three centroids

$$\mu_s = \frac{1}{N} \sum_{i=1}^{N} w_{s,p=0,i}, \tag{2}$$

where N is the total number of reconstructed images at position 0. In the classification phase a class label C is assigned to each of the remaining observations $w_{s,p,i}$, $p \neq 0$, by finding the nearest centroid

$$C = \underset{s \in \{\text{S,M,L}\}}{\arg\min} \| \mu_s - w_{s,p,i} \|_2. \tag{3}$$

3.3. Signal to noise ratio and sample size estimation

To assess the image quality we calculate the signal to noise ratio (SNR) of our multi-channel images for each block averaging length. To begin with a maximum intensity projection along the channels $\mathbf{c}_{\text{S}}$, $\mathbf{c}_{\text{M}}$ and $\mathbf{c}_{\text{L}}$ will be performed for each multi-channel image. Following the notation from the last section the resulting 2D images will be referred to as $\mathbf{c}_{s,p,i}$. The image signal $a_{s,p,i}$ is given by the respective maximal voxel value found in the circular region of interest (ROI) around the corresponding sample position. The image noise $n_{s,p}$ is quantified

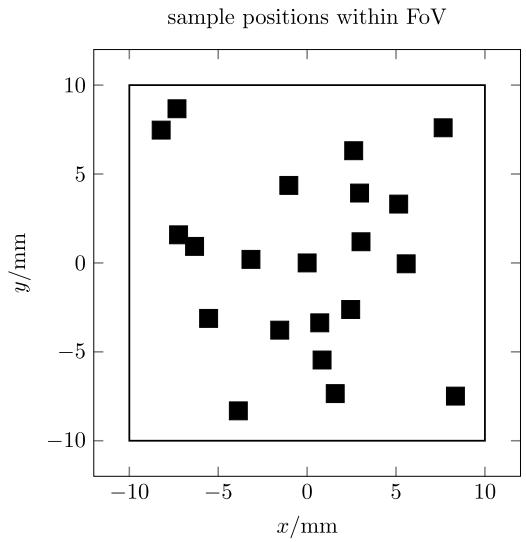

Figure 2. Distribution of the 21 positions listed in table 1 within the FoV (thick rectangle). The size of the markers matches the size of the samples up to a global scaling of the figure.

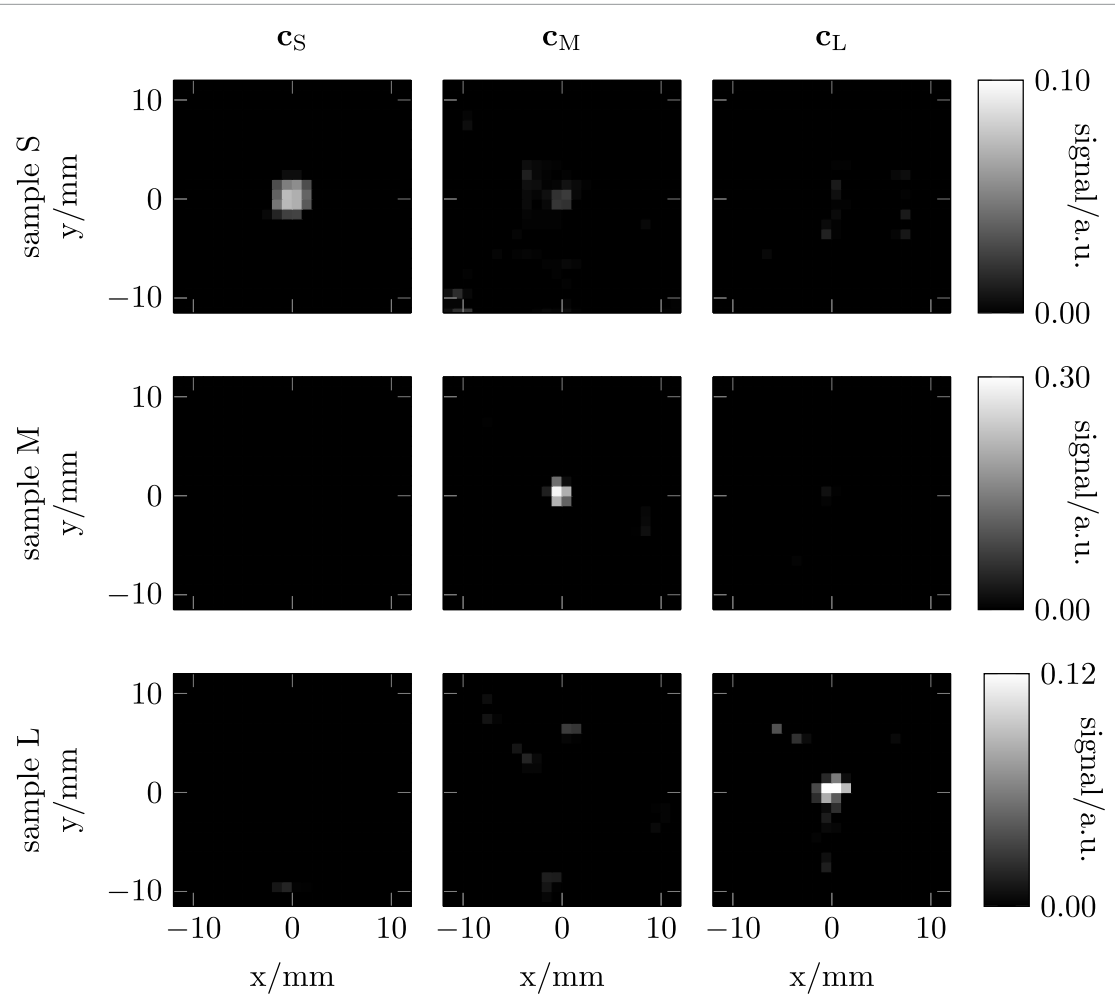

Figure 3. Multi-channel reconstruction $M_{avg} = 10\,000$ of sample S (top row), sample M (middle row), and sample L (bottom row) located at the center (position 0) of the field of view. The signal strength and distribution throughout the channels $\mathbf{c}_S$ (left column), $\mathbf{c}_M$ (middle column), and $\mathbf{c}_L$ (right column) is characteristic for each sample and changes very little with the sample location.

by the standard deviation of all remaining voxel values outside the ROI in all images with equal sample s and location p. The SNR of image i is then simply given by the quotient $a_{s,p,i}/n_{s,p}$ of signal and noise. Similar to the SNR the sample size is estimated by evaluation of the projected images $\mathbf{c}_{s,p,i}$. It is given by the number of voxels $v_{s,p,i}$ inside the ROI with voxel values above half of the image signal $a_{s,p,i}$.

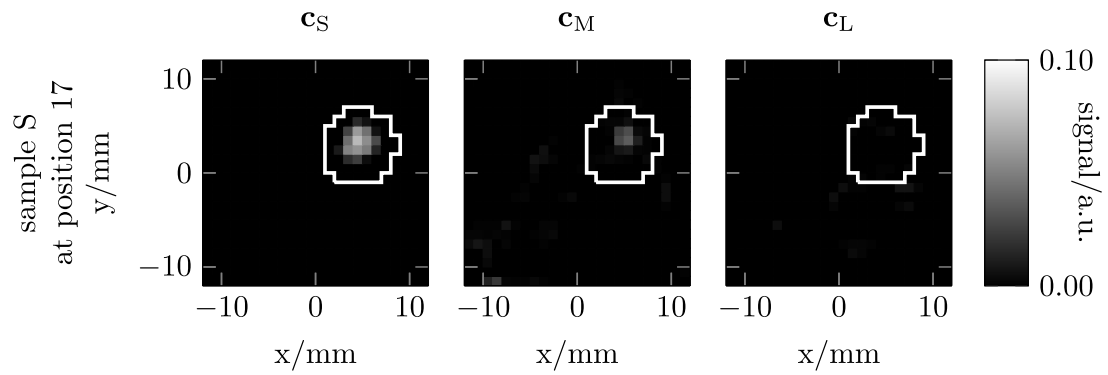

Figure 4. Multi-channel reconstruction $M_{avg} = 10\,000$ of sample at position 17. The ROI is delineated by the white line. Summation of the ROI for each channel yields the weights vector $w = (0.72, 0.11, 0.02)$.

4. Results

4.1. Magnetic particle spectroscopy

MPS measurements are here used to predict the MPI performance of each sample. The tracer response dm/dt plotted against the applied field defines the point spread function (PSF). The height of the PSF indicates the signal intensity of the raw MPI signal, and the full width at half maximum (FWHM) determines the potential image resolution, at least for 1D MPI sequences along the direction of excitation (Croft *et al* 2016). As can be seen from figure 5, the small sample (S) indicates the worst performance, both in terms of signal intensity and resolution, while samples M and L are comparable in terms of indicated performance. We therefore expect a lower signal-to-noise ratio (SNR) from images generated from sample S than from samples M and L. The FWHM decreases with increasing core size, with values of 9.34 mT μ_0^{-1}, 6.57 mT μ_0^{-1} and 6.49 mT μ_0^{-1} for respective samples S, M and L. Hysteresis loops ($m(H)$), generated by integrating the time-domain MPS data, also show the differences in magnetization response among the three samples: the larger particles exhibit an increased phase lag with respect to the excitation field, indicated by the increasing width of the hysteresis loop with size.

4.2. Multi-channel image reconstruction

Observations on a random subset of all reconstructed images show that the multi-channel reconstructions shown in figure 3 are qualitatively representative for most reconstructions. We find a strong signal contribution at the sample location in at least one of the channels of the multi-channel image. Only in some cases does image noise create 'hot' pixels, which are brighter than the sample signal. In the reconstructions of the sample with small sized cores (S) we find the bulk of the signal in the channel $\mathbf{c}_S$ and the remaining signal within channel $\mathbf{c}_M$. As the block averaging length decreases we observe a signal shift from channel $\mathbf{c}_S$ to $\mathbf{c}_M$. Signal within $\mathbf{c}_L$ does occur rarely and therefore seems to be coincidental noise. As for the the sample with medium sized cores (M), we find almost all to all of the signal in channel $\mathbf{c}_M$. Signal within the other channels does occur rarely and is mostly caused by noise. The remaining sample L does behave similarly in that most of the signal is observed in channel $\mathbf{c}_L$. Reconstructions where the above mentioned does not apply occur at positions 5, 6, 14 and 19, which are located close to the corners of the FoV. Here, signal leakage into channel $\mathbf{c}_M$ is visible for samples S and L and an overall drop of the signal intensity can be observed for all samples.

Reconstruction results for the multi-sample phantom are shown in figure 6. The arrangement of the samples for each measurement is shown in the first column of the figure. Sample L is placed in the upper position, sample M is placed in the lower position, and sample S is placed in the left position (see figure 1(c)). The reconstructed channels $\mathbf{c}_S$, $\mathbf{c}_M$ and $\mathbf{c}_L$ are shown in columns two to four. For all combinations one can see that the samples can be spatially resolved and the core size can be separated, with some small signal leakage from the S sample into the M channel which was also observed for the single-sample measurements.

4.3. Core size discrimination

Core size discrimination by classification of the signal weight vectors is possible. The results of the classification are summarized in table 2, which shows the confusion matrices for each block averaging length. Each row of the matrix represents the predicted sample core size while each column represents the true core size. Hence, correct predictions can be found on the diagonal of the matrix and misclassifications can be found off the diagonal. Depending on the block averaging lengths M_{avg} of 10 000, 1000 and 100 the core size is predicted successfully in 96.7%, 92.1% and 88.9% of the cases, respectively. Analyzing the spatial distribution of the misclassified observations, we find a strong accumulation at positions 5, 6, 14 and 19 in the corners of the FoV as shown in

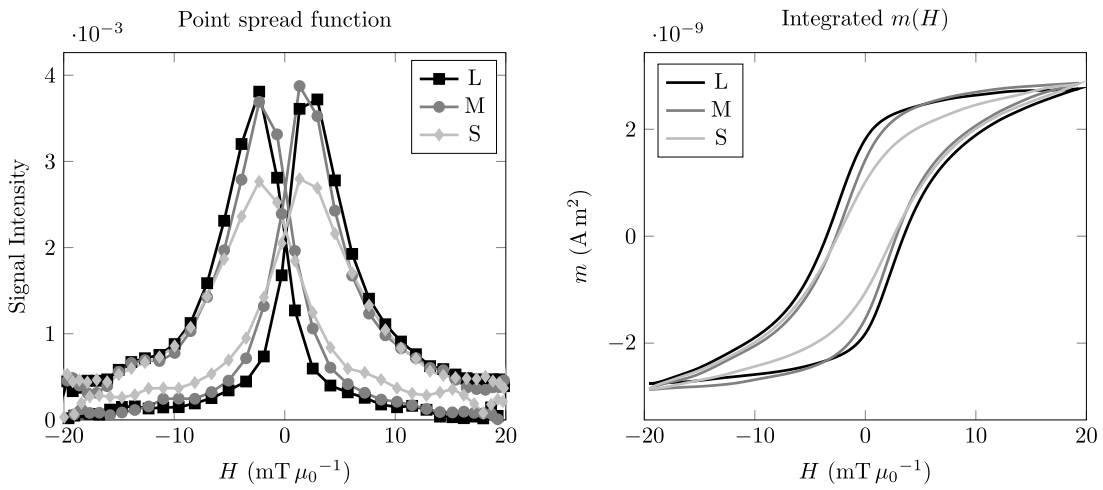

Figure 5. MPI performance of each sample is indicated by the rate of change of the magnetization under an applied AC field. The point spread function (left) of sample S shows decreased peak height and broader FWHM compared to samples M and L. Data points were interpolated and then integrated to produce the $m(H)$ hysteresis loop (right).

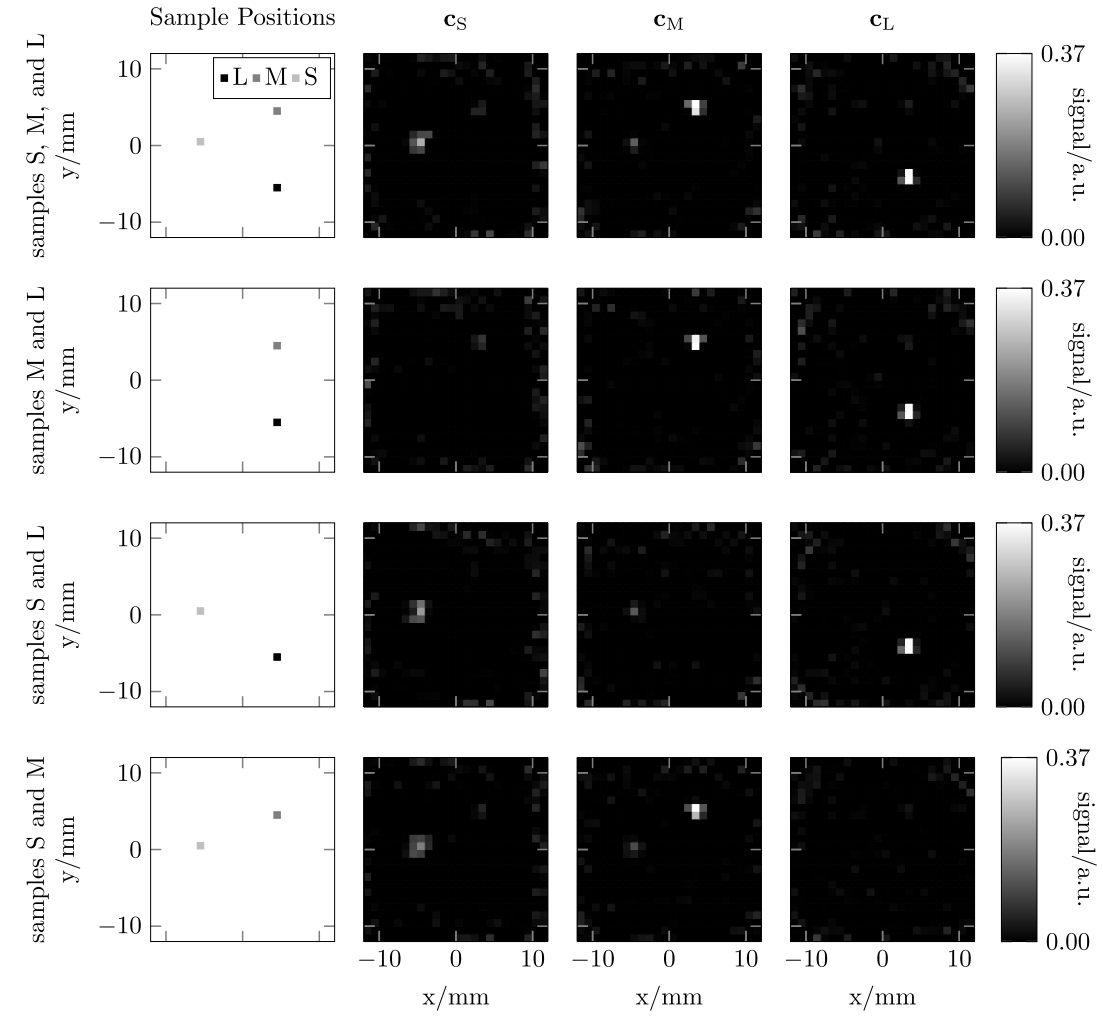

Figure 6. Multi-channel reconstruction with $M_{avg} = 10\,000$ of the multi-sample datasets with all three (top row) or different combinations of two (second to fourth row) samples in the field of view. The location of the samples is indicated in the first column. For each combination the three channels $\mathbf{c}_S$, $\mathbf{c}_M$, and $\mathbf{c}_L$ are shown in the second to fourth columns.

Table 2. A confusion matrix for each averaging block length M_{avg} shows the number of correct assignments in the diagonal of each matrix. The number of false assignments is listed in the off-diagonal elements.

		True core size								
		$M_{avg} = 10\,000$			$M_{avg} = 1000$			$M_{avg} = 100$		
		S	M	L	S	M	L	S	M	L
Class label	S	20	0	2	200	12	38	1950	247	400
	M	0	20	0	0	188	0	43	1753	0
	L	0	0	18	0	0	162	7	0	1600

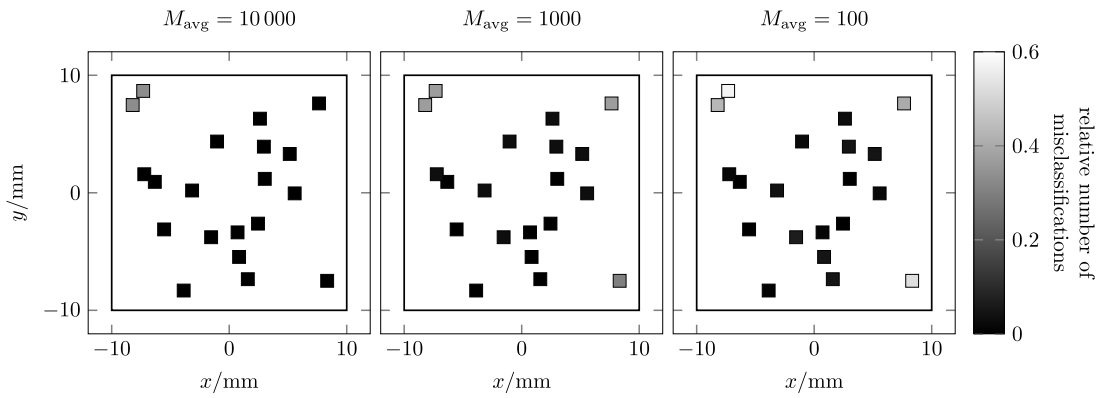

Figure 7. The relative number of misclassifications is shown for all averaging block lengths M_{avg} in dependence on the position of the sample. One observes that most misclassifications occur with the sample close to the corner of the FoV. Moreover, one finds an increase of the relative number of misclassifications with decreasing block averaging length.

figure 7. Restricting our predictions to all positions excluding the aforementioned, one observes a significant improvement of the prediction rates to 100%, 98.3% and 97.5%.

4.4. Signal to noise ratio and sample size estimation

The SNR mainly depends on the sample used and the block averaging length. For $M_{avg} = 10\,000$ we found median SNR values of 40, 260 and 150 for the samples S, M and L, respectively. Similarly, we observed SNR values of 30, 100 and 160 and 20, 60 and 90 for $M_{avg} = 1000$ and $M_{avg} = 100$, respectively.

The estimated sample size too depends on the sample used and the block averaging length. Here, we estimated sample sizes of 8, 3 and 4 voxels for $M_{avg} = 10\,000$ and samples S, M and L, respectively. Similarly, we observed sample sizes of 12, 5 and 6 voxels and 10, 6 and 6 voxels for $M_{avg} = 1000$ and $M_{avg} = 100$, respectively.

5. Discussion

By adapting the multi-channel image reconstruction procedure developed in Möddel *et al* (2018), we have demonstrated simultaneous spatial mapping and nanoparticle size discrimination. To optimize signal-to-noise and resolution, we used highly monodisperse magnetite nanoparticles with core sizes in the range 21.9 nm–27.7 nm. We were consequently able to distinguish between particles that differ in core diameter by as little as 2.5 nm. The two main factors influencing the core size prediction rates were the block averaging length and the spatial position of the sample within the FoV. Raising the block averaging length, which directly relates to the SNR of the MPI measurement, increased the visual quality of the multi-channel images as well as the core size prediction rates. However, more influential was the the sample location. For samples located close to the corners of the drive-field FoV prediction rates dropped down to 33%–66%, which is a direct consequence of the increased signal leakage and reduced signal intensity in the corresponding multi-channel images. We hypothesize that the local excitation trajectory at these positions is the underlying cause for these anomalies as it lacks a strong field reversal like e.g. the excitation trajectory at the central position. For the remaining positions we find predicted rates of above 97.5%, indicating the high sensitivity of our technique.

Limitations naturally arise from the polydispersity of the nanoparticle core sizes. There will be significant overlap in core size among samples, even with low size distribution parameters (<0.1), as seen in figure 8. As a result, there will be some unavoidable signal leakage into other channels, as we have observed. Improving monodispersity, either during the synthesis process or with an additional filtering step, is a key component to improving prediction accuracy.

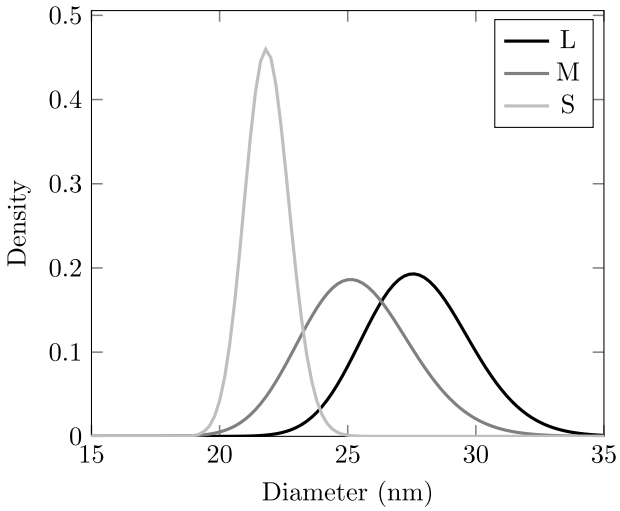

Figure 8. Fits to TEM images indicating the core size distribution of each sample. Fits were performed assuming a log-normal distribution of particle diameters.

Table 3. Calculated equilibrium relaxation times for each sample.

		Brownian relaxation time (s)	Néel relaxation time (s)
Core size	S	2.83×10^{-4}	1.83×10^{-7}
	M	1.55×10^{-4}	6.68×10^{-6}
	L	2.98×10^{-4}	1.63×10^{-4}

We found that the height and FWHM of the PSF extracted from MPS for each nanoparticle sample was able to correctly qualitatively predict their imaging performance. While the height and FWHM of the zero-dimensional MPS peak are known to predict 1D MPI SNR and resolution along the scanning direction, it was unclear if those results could be generalized to 2D excitation sequences. The SNR of sample S in the 2D images is worse than that of samples M and L by at least a factor of 3, while the SNR of samples M and L are comparable, differing by 60% or less. This is consistent with our predictions from MPS, where we found that the peak of the PSF generated from sample S was significantly lower than those of samples M and L, which are about the same height. Similarly, the FWHM from the PSF of sample S was 42%–44% greater than those of the samples M and L, which is consistent with our results that the estimated sample size of sample S is approximately double those of M and L. The FWHM of samples M and L differed by less than 2%, which is reflected by the fact that the estimated sample size of samples M and L is approximately the same in the 2D scans.

During an MPI scan, all particles outside the dynamic region are magnetically saturated. As the field-free point is scanned over the sample, the particles' magnetic moment will rotate in a manner that can be characterized in part by the effective relaxation timescale. The equilibrium relaxation time, whether Brownian ($\tau_B = 3\eta V_h/k_B T$, with viscosity η, hydrodynamic volume V_h, Boltzmann's constant k_B, and temperature T), or Néel ($\tau_N = \tau_0 \exp[KV_c/k_B T]$, with attempt time τ_0, anisotropy K, and core volume V_c) increases with particle size. Relaxation times for each sample are show in table 3. While in reality, the rotation mechanism and effective relaxation time will be dependent on field conditions, we can nevertheless see that the relaxation dynamics are highly sensitive to particle size. In general, larger particles will have a longer relaxation time, and will therefore take longer to begin magnetic reversal. This effect can be seen in figure 5, where the integrated $m(H)$ loop widens with increasing core size. Due to these differences in the reversal dynamics, differences will arise in the frequency spectra, as measured in each sample system matrix, which can then be used to separate and characterize signals from different samples as we have demonstrated.

The signal generated by the particle response can be separated into an adiabatic part, proportional to the derivative of the Langevin function, and a relaxation term (Croft *et al* 2016). The adiabatic term will be dependent on core volume, while the relaxation term will typically be dependent on both core and hydrodynamic size, as shown above. The relative contribution of these two terms has not been theoretically determined, so it is impossible to identify which component contributes most to the signal differences that we observe here.

We do hypothesize that all three samples undergo primarily Néel rotation, after a possible initial Brownian alignment, which is consistent with the fact that the Néel relaxation time is shorter than the Brownian relaxation time for all samples. Following (Shah *et al* 2015), if we assume cubic anisotropy rather than uniaxial anisotropy

for spherical magnetite particles, MNPs first undergo a Brownian alignment to align their nearest easy axis to the field, but then rotate primarily via the Néel mechanism. This interpretation is consistent with results showing that immobilization of particles does not result in a major decrease in signal (Shah *et al* 2015). Under the MPI saturation field, then, all particles large enough to experience Brownian rotation would have aligned easy axes with the field. Larger particles will then have an increased energy barrier KV_c to cross in order to flip their magnetization, which would result in a larger phase lag. This would explain the size-dependent magnetization behavior seen in figure 5. Unfortunately, without samples that all have the same hydrodynamic size (due to the practical difficulties inherent in the coating process), we cannot be confident that this interpretation is correct. However, regardless of which mechanism dominates, it is evident that particle core size has a significant effect on the resulting dynamics.

In this work, we have imaged multiple samples within the same field of view, which is the precursor to multi-contrast *in vivo* experiments with separately functionalized particles. Recently, mixtures of samples were studied with MPS Viereck *et al* (2019), based on spectral discrimination of core and hydrodynamic size. Quantification of nanoparticle mixtures in MPI is significantly more complex than in MPS, and so it is unclear how well the method would work in practice. However, their work indicates that quantifying mixtures of samples may be possible in MPI as well, and would be an interesting future direction for an extension of this work.

6. Conclusion

In this work, we have demonstrated simultaneous spatial mapping and nanoparticle core size discrimination in 2D MPI. This is the first study indicating that optimized MNP tracers, separated by only a few nanometers in core diameter, can be spectrally distinguished. These results could enable a range of new medical imaging applications, wherein optimized MNP cores would be functionalized separately for different purposes, including cancer targeting, circulation in the blood, or coating of devices such as catheters and guide-wires. These separately functionalized particles could then be distinguished in high resolution multi-channel images using this multi-contrast imaging technique.

Acknowledgments

CS was supported by a National Science Foundation Graduate Research Fellowship under Grant DGE-1256082. KMK would like to acknowledge the Alexander von Humboldt Foundation Career Research Award (2016) which made this collaboration possible. TK thankfully acknowledges the financial support by the German Research Foundation (DFG, grant number KN 1108/2-1) and the Federal Ministry of Education and Research (BMBF, grant number 05M16GKA).

ORCID iDs

Carolyn Shasha https://orcid.org/0000-0002-3021-9383
Eric Teeman https://orcid.org/0000-0002-0488-1445
Tobias Knopp https://orcid.org/0000-0002-1589-8517
Martin Möddel https://orcid.org/0000-0002-4737-7863

References

Arami H, Teeman E, Troksa A, Bradshaw H, Saatchi K, Tomitaka A, Gambhir S S, Häfeli U O, Liggitt D and Krishnan K M 2017 Tomographic magnetic particle imaging of cancer targeted nanoparticles *Nanoscale* **9** 18723–30

Bruker Biospin MRI GmbH Ettlingen, Germany 2015 MPI preclinical brochure (Billerica, MA: Bruker)

Coene A, Leliaert J, Liebl M, Loewa N, Steinhoff U, Crevecoeur G, Dupré L and Wiekhorst F 2017 Multi-color magnetic nanoparticle imaging using magnetorelaxometry *Phys. Med. Biol.* **62** 3139

Croft L R, Goodwill P W, Konkle J J, Arami H, Price D A, Li A X, Saritas E U and Conolly S M 2016 Low drive field amplitude for improved image resolution in magnetic particle imaging *Med. Phys.* **43** 424–35

Deissler R J, Wu Y and Martens M A 2014 Dependence of Brownian and Néel relaxation times on magnetic field strength *Med. Phys.* **41** 012301

Ferguson R M, Khandhar A P and Krishnan K M 2012 Tracer design for magnetic particle imaging *J. Appl. Phys.* **111** 07B318

Ferguson R M, Khandhar A P, Arami H, Hua L, Hovorka O and Krishnan K M 2013 Tailoring the magnetic and pharmacokinetic properties of iron oxide magnetic particle imaging tracers *Biomed. Tech./Biomed. Eng.* **58** 493–507

Ferguson R M *et al* 2015 Magnetic particle imaging with tailored iron oxide nanoparticle tracers *IEEE Trans. Med. Imaging* **34** 1077–84

Gleich B and Weizenecker J 2005 Tomographic imaging using the nonlinear response of magnetic particles *Nature* **435** 1214–7

Hensley D, Goodwill P, Croft L and Conolly S 2015 Preliminary experimental X-space color MPI *5th Int. Workshop on Magnetic Particle Imaging* (IEEE) p 1

Kang Y *et al* 2017 Multicolor bioimaging with biosynthetic zinc nanoparticles and their application in tumor detection *Sci. Rep.* **7** 45313

Kemp S J, Ferguson R M, Khandhar A P and Krishnan K M 2016 Monodisperse magnetite nanoparticles with nearly ideal saturation magnetization *RSC Adv.* **6** 77452–64
Khandhar A, Keselman P, Kemp S, Ferguson R, Goodwill P, Conolly S and Krishnan K 2017 Evaluation of peg-coated iron oxide nanoparticles as blood pool tracers for preclinical magnetic particle imaging *Nanoscale* **9** 1299–306
Krishnan K 2010 Biomedical nanomagnetics: a spin through possibilities in imaging, diagnostics, and therapy *IEEE Trans. Magn.* **46** 2523–58
Möddel M, Meins C, Dieckhoff J and Knopp T 2018 Viscosity quantification using multi-contrast magnetic particle imaging *New J. Phys.* **20** 083001
Panagiotopoulos N *et al* 2015 Spio-coating of devices for mpi-guided cardiovascular interventions: proof of principle *5th Int. Workshop on Magnetic Particle Imaging* (IEEE) p 1
Rahmer J, Halkola A, Gleich B, Schmale I and Borgert J 2015 First experimental evidence of the feasibility of multi-color magnetic particle imaging *Phys. Med. Biol.* **60** 1775–91
Rahmer J, Weizenecker J, Gleich B and Borgert J 2009 Signal encoding in magnetic particle imaging: properties of the system function *BMC Med. Imaging* **9** 4
Rauwerdink A and Weaver J 2009 Nanoparticle temperature estimation in combined AC and DC magnetic fields *Phys. Med. Biol.* **54** L51–5
Rauwerdink A and Weaver J 2010 Viscous effects on nanoparticle magnetization harmonics *J. Magn. Magn. Mater.* **322** 609–13
Rauwerdink A, Giustini A and Weaver J 2010 Simultaneous quantification of multiple magnetic nanoparticles *Nanotechnology* **21** 455101
Salamon J *et al* 2016 Magnetic particle/magnetic resonance imaging: *in vitro* MPI-guided real time catheter tracking and 4D angioplasty using a road map and blood pool tracer approach *PLoS One* **11** e0156899
Shah S A, Reeves D B, Ferguson R M, Weaver J B and Krishnan K M 2015 Mixed Brownian alignment and Néel rotations in superparamagnetic iron oxide nanoparticle suspensions driven by an AC field *Phys. Rev.* B **92** 094438
Stehning C, Gleich B and Rahmer J 2016 Simultaneous magnetic particle imaging (MPI) and temperature mapping using multi-color MPI *Int. J. Magn. Part. Imaging* **2** 2365–9033
Utkur M, Muslu Y and Saritas E U 2017 Relaxation-based viscosity mapping for magnetic particle imaging *Phys. Med. Biol.* **62** 3422
Viereck T, Draack S, Schilling M and Ludwig F 2019 Multi-spectral magnetic particle spectroscopy for the investigation of particle mixtures *J. Magn. Magn. Mater.* **475** 647–51
Wawrzik T, Kuhlmann C, Ludwig F and Schilling M 2013 Estimating particle mobility in MPI *Imaging Int. Workshop on Magnetic Particle p* 1
Weizenecker J, Gleich B, Rahmer J, Dahnke H and Borgert J 2009 Three-dimensional real-time *in vivo* magnetic particle imaging *Phys. Med. Biol.* **54** L1–10
Wells J, Paysen H, Kosch O, Trahms L and Wiekhorst F 2018 Temperature dependence in magnetic particle imaging *AIP Adv.* **8** 056703
Zhong J, Schilling M and Ludwig F 2018 Magnetic nanoparticle temperature imaging with a scanning magnetic particle spectrometer *Meas. Sci. Technol.* **29** 115903